RSC Advances

PAPER

View Article Online
View Journal | View Issue

Cite this: *RSC Adv.*, 2021, **11**, 13624

Enhancing the performance of photoelectrochemical glucose sensor *via* the electron cloud bridge of Au in $SrTiO_3$/PDA electrodes†

Yadong Wang,[a] Jinxin Ma,[a] Nan Zhang,[a] Delun Chen,[a] Jinchun Tu,[a] Yang Cao,[ac] Qiang Wu,*[b] Xiaolin Zhang*[c] and Wanjun Hao*[a]

Developing photoelectrochemical biosensors *via* efficient photogenerated-charge separation remains a challenging task in biomolecular detection. In this study, we utilised a simple approach for constructing an efficient photoactive organic–inorganic heterojunction interface composed of $SrTiO_3$ with high photocatalytic activity and polydopamine (PDA) with high biocompatibility and electrical conductivity. Gold nanoparticles with dense electron cloud properties were introduced as a bridge between $SrTiO_3$ and PDA ($SrTiO_3$/Au/PDA). The Au bridge allowed the PDA to uniformly and tightly attach on the surface of $SrTiO_3$ electrodes and also provided a separate transmission channel for electrons from PDA to $SrTiO_3$. The rapidly transmitted electrons were captured by a signal-acquisition system, thereby improving the photocurrent signal output. The 3D hollowed out $SrTiO_3$/Au/PDA biosensor manufactured herein was used for glucose detection. The biosensor achieved ultrahigh sensitivities reaching 23.7 μA mM^{-1} cm^{-2}, an extended linear range (1–20 mM), and a low detection limit (0.012 mM). The excellent results of glucose analysis in serum samples further confirmed the feasibility of the biosensor in clinical applications. In summary, the proposed strategy allowed for the use of an electronic cloud bridge in the construction of glucose biosensors with satisfactory performances, which is promising for the future fabrication of high-performance biosensors.

Received 30th January 2021
Accepted 28th March 2021

DOI: 10.1039/d1ra00812a

rsc.li/rsc-advances

1. Introduction

The use of photoelectrochemistry (PEC) has received increased attention in biosensor development because of its low background noise, low cost, small size, and high sensitivity.[1,2] However, most photoanodes are restricted by material factor limitations, such as narrow light absorption range, low charge separation, and low transfer efficiency. Therefore, the photogenerated electron mobility and biocompatibility of materials are important in constructing PEC electrodes.[3] Photogenerated electrons and holes produced in wide band gap semiconductors, such as TiO_2 and ZnO, were unstable and recombine rapidly, which results in low PEC performance.[4] Therefore, a rapid photoelectron transfer path must be designed and the Fermi energy level of photoelectrodes should be optimized to effectively improve the photoelectrochemical performance of sensors.[5]

$SrTiO_3$ with a perovskite structure has a higher conduction band position than TiO_2, indicating that $SrTiO_3$ has a smaller energy band shift and promotes the transfer of photogenerated electrons better. Thus, $SrTiO_3$ (5–8 cm^2 V^{-1} s^{-1}) has a higher electron mobility than TiO_2 (0.1–4.0 cm^2 V^{-1} s^{-1}).[6] Therefore, $SrTiO_3$ is more suitable to photocatalysis than TiO_2.[7] However, $SrTiO_3$, as a single semiconductor, easily recombines with photogenetic carriers. In addition, the biocompatibility of biosensors is unsatisfactory.[8–10] Thus, improving the biocompatibility of biosensors is a direction worthy of research.[11] Polydopamine (PDA) is a synthetic biomimetic material that has excellent biocompatibility and a stable semiconducting polymer.[12] In PEC sensors, PDA plays an important role in immobilizing enzymes and transferring photoelectrons.[13] Therefore, the low biocompatibility and inefficient charge separation of $SrTiO_3$ can be effectively resolved by combining it with PDA.[14] However, the complex inorganic–organic interface is not conducive to the transmission of photogenerated electrons. For

[a]*Key Laboratory of Advanced Materials of Tropical Island Resources, State Key Laboratory of Marine Resource Utilization in South China Sea, Hainan University, Haikou 570228, P. R. China. E-mail: hwj8899@163.com*

[b]*School of Tropical Medicine and Laboratory Medicine, Key Laboratory of Emergency and Trauma of Ministry of Education, Research Unit of Island Emergency Medicine, Chinese Academy of Medical Sciences (No. 2019RU013), Hainan Medical University, Haikou, 571199, P. R. China. E-mail: wuqiang001001@aliyun.com*

[c]*Key Laboratory of Child Cognition & Behavior Development of Hainan Province, Qiongtai Normal University, Haikou 571127, P. R. China. E-mail: xlzhang0812@gmail.com*

† Electronic supplementary information (ESI) available. See DOI: 10.1039/d1ra00812a

example, a high interface barrier will cause the photogenerated electrons to recombine.[15] Thus, the electronic architectural problem between $SrTiO_3$ and PDA must be resolved.

A low-impedance interface constructed between $SrTiO_3$ and PDA can remarkably improve the transmission efficiency of novel inorganic–organic interfaces. Similarly, Colin Tyznik *et al.*[16] improved the charge separation efficiency by constructing a heterojunction between metal–halide perovskite and organic semiconductor. Constructing a conductive channel between platinum nanoparticles and graphitic carbon can improve the charge-separation ability of the material.[17] This report inspired us to build an electronic cloud bridge to adjust the electronic structure of inorganic–organic interfaces. Noble metal nanoparticles, such as Au and Ag, with high-density electron cloud characteristics can realize effective routes for interface electron transfer.[18] A promising strategy is to directly inject electrons through the strong coupling between nanogold and the unsaturated bond on semiconductor surface.[19] Another approach is the traditional two-step electron transfer in which free electrons are generated by light excitation and then injected into the semiconductor.[20] Therefore, noble metal nanoparticles are more suitable candidates for creating a single electron transmission channel between interfaces by establishing electronic cloud bridges. This approach is expected to address the problem of electron transport and separation between inorganic and organic semiconductors.

In this work, we designed a 3D hollowed out $SrTiO_3$/Au/PDA photoelectrode *via* hydrothermal *in situ* growth, microwave-assisted synthesis, and photopolymerization methods. This photoelectrode efficiently separated photogenerated charges. The assembly strategy provided an independent electron transport channel for a complex inorganic–organic interface *via* Au nanoparticles and effectively achieved charge separation. This biosensor was applied in glucose detection.

2. Experimental section

2.1. Materials

A Ti wire mesh (60 mesh, 0.14 mm wire diameter, and 0.28 mm mesh width) was acquired from Kangwei Metal Wire Mesh Products Co., Ltd (Hebei China). The reagents including strontium hydroxide octahydrate ($Sr(OH)_2 \cdot 8H_2O$, 99.5%), chloroauric acid ($HAuCl_4$), ethylene glycol (EG), ammonia fluoride (NH_4F), dopamine hydrochloride (DA) were purchased from Shanghai Macklin Biochemical Co., Ltd, and 1, 2-propanediol were purchased from Beijing Chemical Reagent Factory, and were analytical grade and were used as received without further purification. Tetrabutylammonium hydroxide (TBAH, 25 wt%) were purchased from Aladdin Industrial Co., Ltd. Glucose oxidase (GOx) (EC 1.1.3.4, 5 kU mg^{-1} from Aspergillus niger) was purchased from Sangon Biotech. Phosphate buffer saline (PBS) was prepared by mixing NaH_2PO_4 and Na_2HPO_4 to adjust the pH. All aqueous solutions were prepared using deionized water (DI) with a resistivity of 18.2 MΩ cm.

2.2. Synthesis of 3D hollowed out TiO_2

The titanium dioxide precursor adopted herein was prepared following a previously described method.[21] At first, a small piece of titanium mesh (20 mm × 10 mm) was treated in a washing solution (volume ratio HF : HNO_3 : H_2O = 1 : 4 : 5) for 10 s. The titanium mesh was separated *via* ultrasonic treatment in isopropanol, acetone, and deionized water for 20 min. At room temperature, the titanium mesh was used as the working electrode, whereas the titanium foil was utilized as the counter electrode for anodizing. The mesh and foil were treated at the constant voltage of 20 V for 90 min. The system reaction solution consisted of 0.3 g of NH_4F, 2 mL of water, and 88 mL of ethylene glycol. The sample was annealed in muffle furnace with a heating rate of 2 °C per minute, and stayed 400 °C for 3 h.

2.3. Synthesis of 3D hollowed out $SrTiO_3$

The as-synthesized 3D hollowed out TiO_2 was used as the template for synthesizing 3D hollowed out $SrTiO_3$ *via* the hydrothermal *in situ* growth method. During the typical synthesis, the 3D hollowed out TiO_2 was immersed in a Teflon-sealed stainless steel autoclave loaded with solutions of $Sr(OH)_2 \cdot 8H_2O$ (1 mmol) in 17 mL of deionized water, 2 mL of 1,2-propanediol, and 2 mL of tetrabutylammonium hydroxide solution (TBAH, 25 wt%) and then heated at 180 °C for 12 h. The obtained samples were washed three times with 0.1 M HCl solution and deionized water and then dried at 50 °C for 30 min.

2.4. Synthesis of 3D hollowed out $SrTiO_3$/PDA

The PDA on the $SrTiO_3$ electrode surface was UV photopolymerized by immersing the electrode in a stirred PBS (pH = 6.0) containing 10 mM DA for 4 h. These steps were repeated on the other electrode side. Finally, the electrode was rinsed with deionized water and then dried at 50 °C for 30 min.

2.5. Synthesis of 3D hollowed out $SrTiO_3$/Au/PDA

$SrTiO_3$/Au electrodes were prepared *via* microwave-assisted polyol heating. First, a mixed solution was prepared in an Erlenmeyer flask containing 30 mL of ethylene glycol, 3 mL of deionized water, and 2 mL of $HAuCl_4$ (0.5 mg mL^{-1}). The mixture was stirred well for 10 min. The strontium titanate substrate was then microwave-digested in this mixed solution for 1 min and finally rinsed with ethanol and H_2O. $SrTiO_3$/Au/PDA electrodes were prepared by loading the PDA with the $SrTiO_3$/Au electrodes following the method outlined above.

2.6. Immobilization of glucose oxidase

The 3D hollowed out $SrTiO_3$/Au/PDA electrodes were placed in a 4 °C environment for 30 min in advance. Subsequently, 5 μL of GOx solution (PBS pH = 7.4) was evenly dispersed on the electrode surface, and then the electrodes were dried at 4 °C for 24 h. These steps were repeated for the other electrode side.

2.7. PEC measurements

The electrochemical investigations and biosignal conversions were performed using an electrochemical workstation (CHI Instruments, Chenhua CHI 660E, Shanghai, China) with a 500 W xenon lamp (Beijing Zhongjiao Jinyuan Technology Co., Ltd, China). The test system was used with a three-electrode system (a Pt sheet was used as the counter electrode and saturated Ag/AgCl was used as the reference electrode, bias of 0.4 V, PBS pH = 7.4). During the measurement, the electrode was subjected to an optical density of 100 mW cm^{-2}.

2.8. Characterization

Powder X-ray diffraction (XRD) patterns were recorded on a Panaltical X'Pert-pro MPD X-ray power diffractometer using Cu Kα radiation (λ = 1.54056 Å). Field-emission scanning electron microscopy (FEI Nano SEM 430) was used to acquire SEM images. Transmission electron microscope (TEM) was performed on JEOL JEM-2100F electron microscope operated at 200 kV. X-ray photoelectron spectroscopy (XPS) spectra were recorded using an ESCALAB 250 Xi XPS system of Thermo Scientific, where the base pressure in analysis chamber was 1.5 $\times$ 10^{-9} mbar and the X-ray spot was 500 μm. UV-Vis diffuse reflection absorption spectra of the samples were obtained by a Varian Cary 5000 UV-Vis spectrometer equipped with an integrating sphere accessory and $BaSO_4$ as a reference material.

3. Results and discussion

3.1. Design guidelines and microstructure of the electrodes

The typical procedure for synthesizing the PEC sensor is presented in Scheme 1. The 3D hollowed out TiO_2 nanowire clusters were first obtained *via* Ti mesh anodization because the 3D hollow Ti mesh structure has a low steric hindrance for biological reactions.[21,22] Scanning electron microscopy (SEM) revealed a highly ordered array of nanowire clusters in the synthesized TiO_2 (Fig. 1(a)). Moreover, a single unit presented a bird's nest-like nanowire cluster structure. This particular structure provided convenient conditions for complete $SrTiO_3$ conversion (Fig. 1(a)). The synthesized TiO_2 nanowire cluster array was hydrothermally converted to a $SrTiO_3$ nanostructure. As shown in Fig. 1(c), the synthesized $SrTiO_3$ had highly ordered nanoarrays similar to the morphology of the TiO_2 precursor. At high magnifications, $SrTiO_3$ cubes were observed to have piled up into hills. In alkaline environments, Sr^{2+} can chemically react with TiO_2 to generate $SrTiO_3$ *via* dissolution–precipitation. In this process, the nanowire TiO_2 was first dissolved around the titanium mesh to form a liquid phase ($Ti(OH)_n^{(n-4)-}$) and then participated in the nucleation and ion-mediated growth of $SrTiO_3$. At this point, *in situ* $SrTiO_3$ growth had been completed. The growth mechanism can be expressed by the following reactions (eqn (1) and (2)):[23]

$$TiO_2(s) + (n-4)OH^-(aq) + 2H_2O(l) \rightarrow Ti(OH)_n^{(n-4)-}(aq)\ (n = 4\text{–}6), \quad (1)$$

$$Ti(OH)_n^{(n-4)-}(aq) + Sr^{2+}(aq) + (6-n)OH^-(aq) \rightarrow SrTiO_3(s) + 3H_2O(l). \quad (2)$$

Subsequently, PDA with high biocompatibility was loaded onto the surface of the synthesized $SrTiO_3$ *via* photopolymerization. According to the literature, photopolymerization is the effective method for preparation of PDA. Firstly, the photopolymerization method can functionalize many flat, curved, and even irregular substrates.[24] Secondly, no catalyst is needed in the polymerization process.[25] Thirdly, robust and well-defined polymer brushes can be directly transplanted onto various surfaces.[26,27] As shown in Fig. 1(d), PDA was randomly distributed on the surface of $SrTiO_3$ nanoarrays, and its adhesion on the surface was evidently poor. PDA was anchored on the surface of $SrTiO_3$ nanoarrays after being loaded with gold *via* microwave-assisted polyol heating (Fig. 1(b)). The distribution of PDA after adding gold was more uniform than that in samples without gold. This uniform distribution makes better contact between the PDA and the substrate, which is conducive to enhancing the transmission of photogenerated electrons.[28] Hence, the problem of uneven PDA distribution was resolved by adding gold. As shown in the enlarged schematic of nanoarray monomers in Scheme 1, PDA was tightly arranged on the surface when gold was added. By contrast, the arrangement was loose when gold was not added. This is due to the extremely high surface energy of gold promoted the close integration of PDA and $SrTiO_3$.[29,30] In addition, the high-density electron cloud on the gold surface provided a high-speed bridge for photogenerated electrons to quickly transfer to the electrode.

Transmission electron microscopy (TEM) revealed that the $SrTiO_3$/Au/PDA composite had uniformly sized approximately 20 nm in size (Fig. 1(f)). The composition of the composite was characterized *via* HRTEM (Fig. 1(e)), EDX (Fig. S1 in ESI†), and mapping (Fig. 1(g)). As shown in Fig. 1(g), the $SrTiO_3$/Au/PDA had a uniform distribution of Ti, Sr, O, N, and Au, thereby confirming the formation of $SrTiO_3$, Au, and PDA. Moreover, Ti (17.23%), Sr (12.71%), O (57.79%), N (11.52%), and Au (0.72%) elements were found in the $SrTiO_3$/Au/PDA composite (Fig. S1 in ESI†), indicating that the $SrTiO_3$ substrate formed and Au and PDA were uniformly loaded onto its surface. The $SrTiO_3$/Au/PDA composite material had some clear lattice fringes (Fig. 1(e)), including lattice fringes of 0.273, 0.39, and 0.233 nm, corresponding to the $SrTiO_3$(110), $SrTiO_3$(100), and Au(111) planes, respectively. Amorphous regions were clearly observed around these lattice fringes, corresponding to PDA. According to HRTEM images (Fig. S2 in ESI†), the $SrTiO_3$/Au/PDA composite had a richer amorphous region than the $SrTiO_3$/PDA composite. This result also demonstrated that Au made the PDA to uniformly distribute in $SrTiO_3$ nanoarrays.

3.2. Characterization of the electrodes

The composition of the material was further analyzed *via* X-ray diffraction (XRD). First, the diffraction peaks of titanium dioxide were characterized (Fig. S3 in ESI†). All diffraction peaks

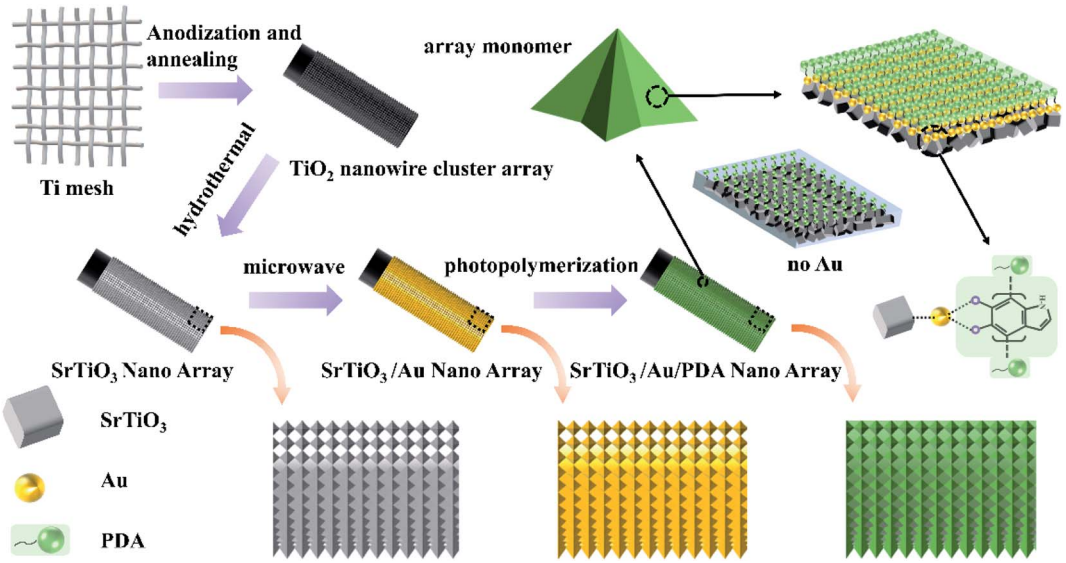

Scheme 1 Process of preparing the 3D hollowed out $SrTiO_3$/Au/PDA PEC sensor and schematic of its microscopic appearance.

detected were matched to typical TiO_2 in the anatase phase (JCPDS: 21-1272)[31] and pure Ti phase (JCPDS: 44-1294),[32] indicating that the synthesized precursor was pure anatase TiO_2. Subsequently, the prepared strontium titanate material and its composite with gold and PDA were tested (Fig. 2(a)). The diffraction peaks of the prepared strontium titanate perfectly matched the pure phases of $SrTiO_3$ phase (JCPDS: 035-0743)[6] and Ti phase. No other diffraction peaks were found, especially the diffraction peak of TiO_2. The XRD of the composite material loaded with amorphous PDA was not different from that of $SrTiO_3$, suggesting that the crystal structure of $SrTiO_3$ was not affected by PDA. Finally, the diffraction peaks of Au (JCPDS: 04-0784)[18] could not be clearly analyzed *via* XRD because their peaks were weak and close to those of Ti. The elemental states of all prepared materials were tracked *via* X-ray photoelectron spectroscopy (XPS). As shown in Fig. 2(b), $SrTiO_3$ only contained Sr, Ti, and O elements, $SrTiO_3$/PDA only contained Sr, Ti, O, and N elements, and $SrTiO_3$/Au/PDA only contained Sr, Ti, O, N, and Au elements. This result also proved that the $SrTiO_3$/Au/PDA composite was successfully and accurately prepared. The binding energy for Sr 3d peaks (Fig. 2(c)) distributed at 132.9 and 134.5 eV were matched to Sr $3d_{5/2}$ and Sr $3d_{3/2}$, respectively, corresponding to Sr^{2+}.[4] The peaks located at 485.15 and 463.95 eV attributed to Ti $2p_{3/2}$ and $2p_{1/2}$, respectively, matched the binding energy of Ti^{4+} (Fig. 2(d)).[33] In addition, the prepared $SrTiO_3$/PDA and $SrTiO_3$/Au/PDA material had slight shifts in the peaks of Sr 3d and Ti 2p. These shifts were attributed to the influence of Au and PDA on the electronic state of $SrTiO_3$. The N 1s spectra (Fig. 2(e)) could be separated into four peaks at 398.7 (==N–), 399.9 (–NH–), 400.7 ($–NH_2$), and 401.8 eV ($–NH_3^+$).[34] The high-resolution spectra of C 1s is shown in Fig. S4 (ESI†). The peaks centered at 284.8 ± 0.1 eV, 286.1 ± 0.3 eV and 288.9 ± 0.1 eV could be assigned to the benzene, C–O or C–N and O–C=O, respectively.[35,36] From their percentages in the samples (Table S1 in ESI†), it can be seen that, in comparison with $SrTiO_3$/Au (28.57%), the relative contents of C–O or C–N in $SrTiO_3$/Au/PDA (62.60%) obviously increased. This result also confirmed that the PDA was successfully fixed to the electrode. The detection of these amine functional groups indicated that the PDA layer was successfully loaded onto the surface of the 3D hollowed out $SrTiO_3$. The peaks of Au 4f were concentrated at the binding energies of 83.9 and 87.6 eV, corresponding to Au $4f_{7/2}$ and $4f_{5/2}$, respectively (Fig. 2(f)). In addition, the peak of Au $4f_{7/2}$ slightly shifted from the standard value of Au element. This shift was attributed to the interaction of Au with $SrTiO_3$ and PDA. These results confirmed that the 3D hollowed out $SrTiO_3$/Au/PDA composite was successfully synthesized.

3.3. Electrochemical measurement of the electrodes

The successful implementation of the gold electronic cloud bridge design was confirmed in a series of analyses (Fig. 3). UV-vis diffuse reflectance spectra are important and powerful indicators of the optical characteristics of materials. The light-absorption capacity of the prepared $SrTiO_3$, $SrTiO_3$/PDA, and $SrTiO_3$/Au/PDA materials was investigated *via* UV-vis diffuse reflectance spectra (Fig. 3(a)). $SrTiO_3$/Au/PDA had the strongest light absorption in both ultraviolet and visible light regions. $SrTiO_3$/PDA had the second strongest light absorption. This result indicated that $SrTiO_3$/Au/PDA had the best photodynamic performance. This excellent performance was attributed to the enhancement of PDA load on the surface of $SrTiO_3$ upon the addition of gold nanoparticles and the successful construction of the gold electronic cloud bridge. Changes in the band gap of the samples were calculated *via* the Tauc plot method by using the following equation:

$$(\alpha h\nu)^{1/2} = A(h\nu - E_g), \quad (3)$$

where α is absorbance index, h is Planck constant, ν is frequency, A is a constant, and E_g is semiconductor band gap. In

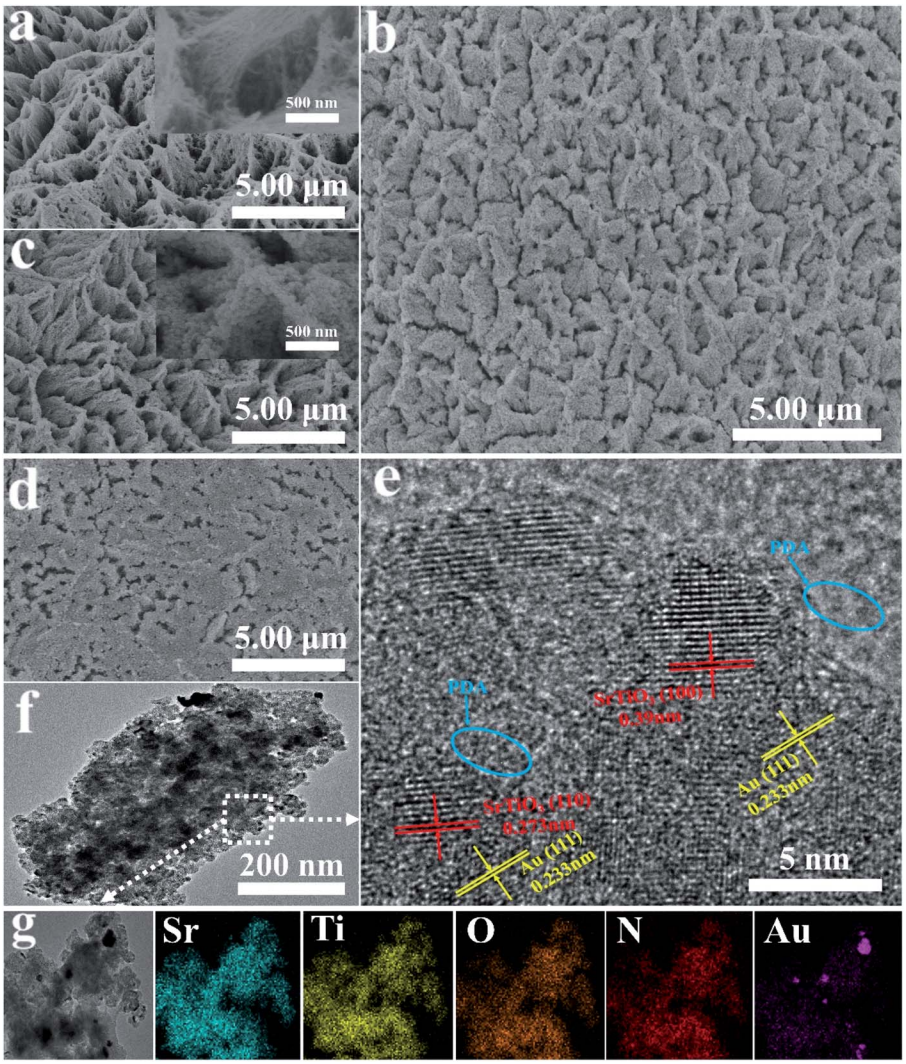

Fig. 1 SEM images of (a) TiO_2, (b) $SrTiO_3$/Au/PDA, (c) $SrTiO_3$, and (d) $SrTiO_3$/PDA. (e) HRTEM image of $SrTiO_3$/Au/PDA. (f) TEM image of $SrTiO_3$/Au/PDA. (g) Mapping of $SrTiO_3$/Au/PDA (from left to right: Sr, Ti, O, N, and Au).

this study, absorbance was used as a parameter to replace α. The relationship between $(\alpha h\nu)^{1/2}$ and $h\nu$ is depicted in Fig. 3(b). The band gap evidently decreased from $SrTiO_3$ (3.245 eV) and $SrTiO_3$/PDA (3.240 eV) to $SrTiO_3$/Au/PDA (3.220 eV) possibly because of the coupling of semiconductor energy levels. In general, this decrease in band gap is helpful in improving the performance of PEC sensors.

The efficiency of surface charge transfer was evaluated *via* the EIS test method. As shown in Fig. 3(c), in this model, R_s represent the solution resistance, and R_{ct} represent the charge transfer resistance at the semiconductor/electrolyte interface. Notably, compared with pristine $SrTiO_3$ (12 705 Ω) and $SrTiO_3$/PDA (10 439 Ω), the value of R_{ct} (5917 Ω) for $SrTiO_3$/Au/PDA is dramatically decreased, which means the charge transfer resistance inside the $SrTiO_3$/Au/PDA electrode is much smaller than that of $SrTiO_3$ and $SrTiO_3$/PDA. The above results demonstrate that the coating of Au can accelerate the interfacial transfer and separation of charge carriers of $SrTiO_3$/Au/PDA. The ability of $SrTiO_3$/Au/PDA to efficiently transfer photogenerated electrons proved the existence of the gold electronic cloud bridge. The PEC performance of the prepared materials was evaluated by observing time-dependent current under on and off light switching. In Fig. 3(d), $SrTiO_3$/Au/PDA had the highest light-absorption performance and the highest charge-separation efficiency, resulting in the highest photocurrent value. Moreover, the photocurrent value of $SrTiO_3$/Au/PDA further increased because of the contribution of Au (Fig. S5 in ESI†). This result also confirmed that the gold electronic cloud bridge was successfully constructed between $SrTiO_3$ and PDA.

The electronic lifetime and carrier density (N_D) of the materials were characterized *via* open-circuit potential (OCP) and Mott–Schottky plots, respectively, to understand further how the performance and electronic properties of PEC were improved. According to the results of OCP tests, electronic lifetime was calculated using eqn (4):[37]

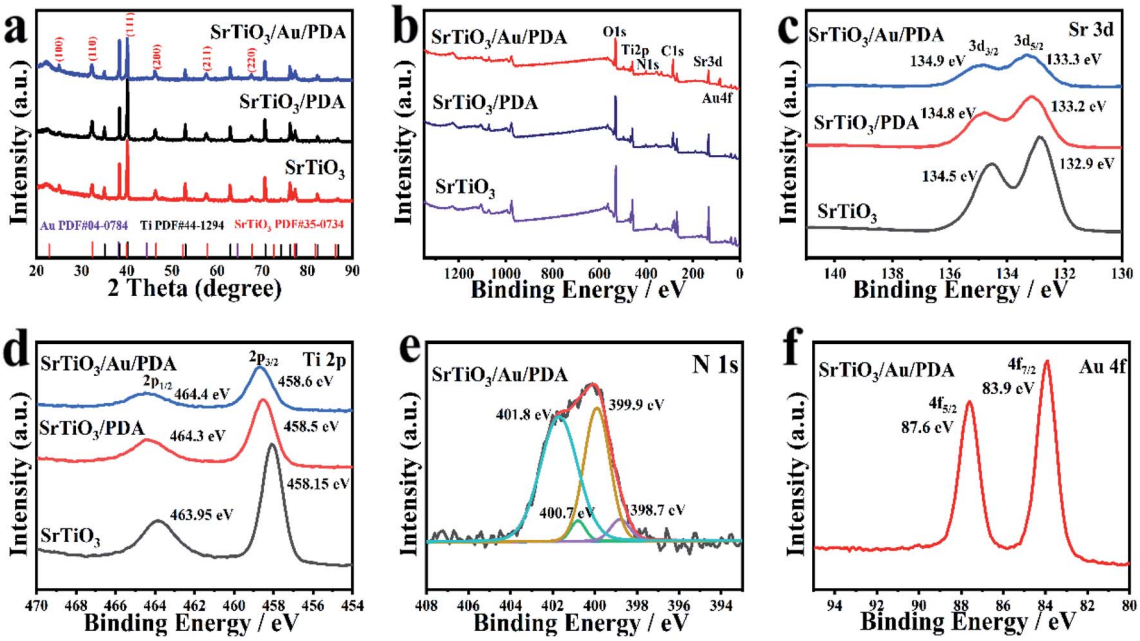

Fig. 2 (a) XRD of $SrTiO_3$, $SrTiO_3$/PDA, and $SrTiO_3$/Au/PDA. (b) Full-range XPS spectra of $SrTiO_3$, $SrTiO_3$/PDA, and $SrTiO_3$/Au/PDA. (c–f) Amplification local XPS of Sr, Ti, N, and Au.

$$\tau = \frac{KT}{e}\left(\frac{\mathrm{d}V_{OC}}{\mathrm{d}t}\right)^{-1}, \quad (4)$$

where τ is the potential dependent photoelectron lifetime, k is Boltzmann's constant, T is temperature, e is the charge of a single electron, and V_{oc} is the open-circuit voltage at time t. $SrTiO_3$/Au/PDA evidently had the longest electron lifetime that greatly contributed to its photoelectric performance (Fig. 3(e)).

The Mott–Schottky equation (eqn (5)) supported the carrier density (N_D) calculated by the Mott–Schottky plots:[37]

$$\frac{1}{C^2} = \frac{2}{N_D e \varepsilon_0}\left[(U_S - U_F) - \frac{KT}{e}\right], \quad (5)$$

where C is the space charge capacitance in the semiconductor, N_D is the electron carrier density, e is the elemental charge value, ε_0 is the permittivity of the vacuum, ε is the relative permittivity of the semiconductor, U_S is the applied potential, T

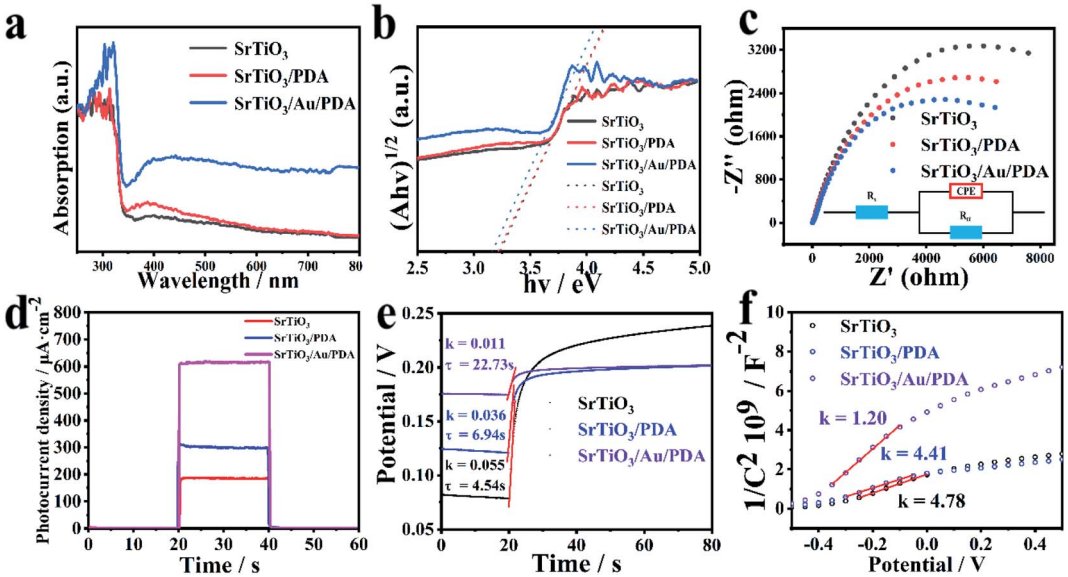

Fig. 3 $SrTiO_3$, $SrTiO_3$/PDA, and $SrTiO_3$/Au/PDA PEC sensors. (a) UV-vis absorption spectra. (b) Plots of $(\alpha h\nu)^{1/2}$ and $h\nu$. (c) EIS Nyquist plots at 0.4 V *vs.* Ag/AgCl under light radiation in 0.1 M PBS (pH = 7.4). (d) Photocurrent response. (e) Open-circuit potential plots. (f) Mott–Schottky plots.

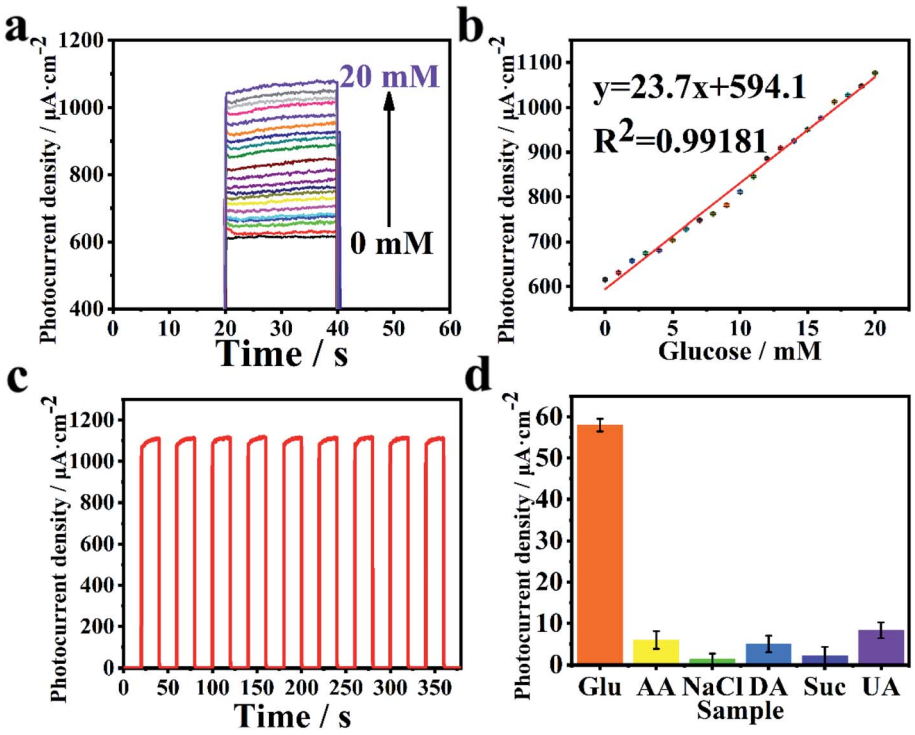

Fig. 4 3D hollowed out $SrTiO_3$/Au/PDA/GOx PEC sensor. (a) Photocurrent responses at different glucose concentrations (0–20 mM) in 0.1 M PBS (pH = 7.4). (b) Calibration curve of glucose concentration and photocurrent density. (c) Stability detection curve in 0.1 M PBS (pH = 7.4) at 20 mM of glucose. (d) Histogram of the results of anti-interference analysis (3 mM Glu and 0.3 mM each of AA, NaCl, DA, Suc, and UA).

is temperature, and k is the Boltzmann constant. Among all samples, $SrTiO_3$/Au/PDA had the largest carrier density (Fig. 3(f)). The increase in electrical conductivity during the material recombination process was confirmed by the substantial enhancement in carrier density that accelerated the transfer of photogenerated electrons. In general, $SrTiO_3$/Au/PDA exhibited extremely high charge separation efficiency that directly benefitted from the successful construction of the gold electronic cloud bridge.

3.4. Sensing measurements of the biosensors

Owing to the excellent performance of PEC under light radiation, the 3D hollowed out $SrTiO_3$/Au/PDA material was selected as the primary photoelectrode material for PEC sensing detection. The performance of the biosensor in PEC detection was evaluated. GOx was selected as the representative enzyme for detecting glucose concentration. Sensitivity, linear range, and limit of detection (LOD) are important indicators of sensor performance. The ability of the $SrTiO_3$/Au/PDA photoelectrode to detect different glucose concentrations was examined (Fig. 4). Results showed that photocurrent gradually increased as glucose concentration increased (Fig. 4(a)). This trend arose because of the strong reducing $FADH_2$ (Flavine adenine dinucleotide, reduced), which was produced during glucose oxidation. Moreover, $FADH_2$ consumed the photogenerated holes in the photoelectrode and assisted in enhancing the photocurrent. The calibration curve of photocurrent and glucose concentration was analyzed (Fig. 4(b)). Results confirmed the excellent

Table 1 Comparison of the biosensors constructed in previous works and the biosensors developed in this study in terms of several performance indicators

PEC sensors	Linear range (mM)	LOD (mM)	Sensitivity (μA mM^{-1} cm^{-2})	Ref.
TiO_2 NTs/PDA/N–GQDs	0–11	0.016	13.6	33
R/A-TiO_2@GOx	1–20	0.019	5.71	41
ITO/TiO_2–MoS_2–GOx	0.1–10	0.015	0.81	42
FTO/Fe_2O_3–NB–PDA–GDH	0–2	0.025	7.36	43
GOx/CdTe	0.1–11	0.04	—	44
a-MoS_x/RGO/ITO	0.15–16	0.098	—	45
3D hollowed out $SrTiO_3$/PDA	0–20	0.017	8.9	This work
3D hollowed out $SrTiO_3$/Au/PDA	0–20	0.012	23.7	This work

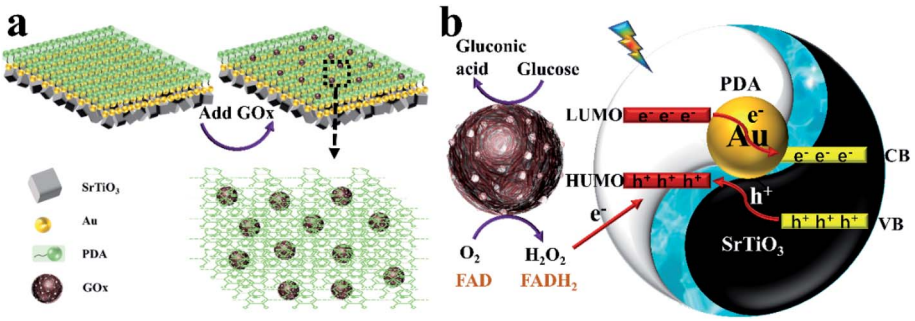

Scheme 2 (a) Modification of GOx on the 3D hollowed out $SrTiO_3$/Au/PDA. (b) Mechanism by which gold accelerates photogenerated electron transfer.

biosensing performance of the 3D hollowed out $SrTiO_3$/Au/PDA (Fig. 4). The biosensor had wide linear range of 1–20 mM, a high sensitivity of 23.7 μA mM^{-1} cm^{-2}, and a low LOD of 0.012 mM (S/N = 3).

The base material (3D hollowed out $SrTiO_3$/PDA) was used for glucose detection to confirm its excellent PEC performance objectively. All test methods and conditions for the 3D hollowed out $SrTiO_3$/PDA PEC sensor were exactly the same as those for the 3D hollowed out $SrTiO_3$/Au/PDA PEC sensor. The results of the comparison of these sensors, including photoelectric performance curves and calibration curves, are exhibited in Fig. S6 (ESI†). Although the 3D hollowed out $SrTiO_3$/PDA PEC sensor had the same linear detection range as the 3D hollowed out $SrTiO_3$/Au/PDA PEC sensor, its sensitivity was only 37.55% of that of the 3D hollowed out $SrTiO_3$/Au/PDA PEC sensor. The excellent PEC performance of the 3D hollowed out $SrTiO_3$/Au/PDA PEC sensor was attributed to the contribution of Au to electron transfer. In addition, the influence of PDA on the performance of PEC sensors is also explored. As shown in Fig. S7 (ESI†), the thickness of PDA of $SrTiO_3$/Au/PDA is about 3 nm, while the thickness of PDA of $SrTiO_3$/Au/PDA (excessive PDA) is 8–10 nm, and the distribution is uneven. Subsequently, $SrTiO_3$/Au/GOx and $SrTiO_3$/Au/PDA (excess PDA)/GOx PEC sensors were used for glucose detection. The performance of PEC sensors $SrTiO_3$/Au/GOx and $SrTiO_3$/Au/PDA (excess PDA)/GOx for glucose detection was evaluated (Fig. S8 in ESI†). The results show that the sensitivity of $SrTiO_3$/Au/GOx and $SrTiO_3$/Au/PDA (excess PDA)/GOx to glucose detection is 43.04% and 33.80% of the sensitivity of $SrTiO_3$/Au/PDA/GOx, respectively. Therefore, it can be concluded that PDA greatly improves the glucose detection performance of the sensor, which is attributed to the fact that PDA provided an excellent biocompatible environment for enzymes. Furthermore, the promotion of charge separation and transfer had a very positive effect on sensitivity. Therefore, the gold electron cloud bridge played an extremely important role in sensitivity improvement.

The stability of the 3D hollowed out $SrTiO_3$/Au/PDA as a PEC biosensor was tested in nine cycles of intermittent light radiation in a solution with 20 mM of glucose. After nine cycles, the photocurrent of the 3D hollowed out $SrTiO_3$/Au/PDA/GOx biosensor had 99.85% of its initial value, which shows remarkable stability in a short time. To monitor the long-term stability of the biosensor, we performed 20 mM glucose measurement every 1 day (stored at 4 °C for the rest of the time). As shown in Fig. S9 (ESI†), the photocurrent of the 3D hollowed out $SrTiO_3$/Au/PDA/GOx biosensor had an initial value of 99.44% after 10 days. Results showed that the PEC biosensor had excellent stability (Fig. 4(c)), confirming that PDA provided a good biocompatible environment for the enzyme that greatly enhanced the enzyme catalytic activity. The specificity of electrodes in biological testing is critical to detection results. Hence, several interfering substances, such as ascorbic acid (AA), sodium chloride (NaCl), dopamine (DA), sucrose (Suc), and uric acid (UA), were individually added after glucose (Glu). The PEC biosensor exhibited excellent anti-interference ability (Fig. 4(d)). In addition, the sensing mechanism of glucose is described in the ESI.† Compared with the biosensor developed in a previous work (Table 1), the PEC biosensor developed herein had better and satisfactory results in terms of sensitivity and linear range.

The detection ability of the 3D hollowed out $SrTiO_3$/Au/PDA/GOx sensor was tested by analyzing glucose concentration in human serum samples. Five human serum samples with known blood glucose concentrations were obtained at The First Affiliated Hospital of Hainan Medical University. Subsequently, the human serum samples were diluted 50 times with 0.1 M PBS. The glucose concentration of these samples was measured using the 3D hollowed out $SrTiO_3$/Au/PDA/GOx PEC sensor. Results showed that the concentration detected by the sensor was consistent with the known glucose concentration (Table S2 in ESI†). Moreover, the serum detection recovery rate ranged from 98.487% and 100.831%, which was within the acceptable range (Table S2 in ESI†). This result supported the claim that the 3D hollowed out $SrTiO_3$/Au/PDA PEC sensor constructed herein can be used in detecting glucose concentrations in actual human blood samples.

3.5. Sensing mechanism of the 3D hollowed out $SrTiO_3$/Au/PDA/GOx biosensor

As shown in Scheme 2, the path of the 3D hollowed out $SrTiO_3$/Au/PDA PEC sensor modified by GOx and the gold electron cloud bridge accelerated the transfer mechanism of photogenerated electrons. In Scheme 2(a), GOx was tightly wrapped in the PDA layer of the PEC sensor. Therefore, the highly

biologically active PDA created an efficient catalytic environment for GOx. In Scheme 2(b), when light radiation reached a certain intensity, the PDA molecule changed from the ground state to the excited state because a transition behavior of π–π*. Afterward, the electrons at the excited state transitioned from the highest occupied molecular orbital of PDA to the lowest unoccupied molecular orbital (LUMO) with a high energy level. The excited electrons enriched in LUMO thermodynamically transferred to the conduction band (CB) of $SrTiO_3$ because the LUMO of PDA was about −1.468 eV (*vs.* NHE)[38] and the CB of $SrTiO_3$ was approximately −0.8 eV (vs. NHE).[39] The transfer of photogenerated electrons induced the photogenerated holes to transfer in the opposite direction and finally annihilated by glucose oxidation.[40] In this process, sensitivity can be effectively improved by accelerating the transfer of photogenerated electrons. Therefore, elemental gold with extremely dense electron clouds has an indispensable role in the rapid transfer of photogenerated electrons. As an electronic bridge, gold provides a fast channel for the transfer of photogenerated electrons and promotes the separation and transfer of photogenerated charges, thereby substantially improving the photoelectrochemical performance of the 3D hollowed out $SrTiO_3$/Au/PDA.

4. Conclusion

A 3D hollowed out $SrTiO_3$/Au/PDA composite material was successfully manufactured in this study. This material was characterized *via* SEM, XPS, XRD, TEM, EDX, mapping, UV-vis spectroscopy. The construction of the gold electronic cloud bridge at the $SrTiO_3$–PDA interface endowed the 3D hollowed out $SrTiO_3$/Au/PDA with excellent photoelectrochemical performance and efficient charge separation ability. As a novel type of PEC biosensor, the performance of the 3D hollowed out $SrTiO_3$/Au/PDA/GOx electrode in glucose detection was tested. This electrode had a low LOD of 0.012 mM and an ultrahigh sensitivity of 23.7 μA mM^{-1} cm^{-2} within a wide linear range of 1–20 mM. In short, the biosensor exhibited extremely high sensitivity. The results provide a novel idea for designing efficient photocatalytic devices.

Conflicts of interest

There are no conflicts to declare.

Acknowledgements

This research was financially supported by the National Natural Science Foundation of China (no. 51762012, 81860373, 51862006 and 82060386), the Finance Science and Technology Project of Hainan Province (no. ZDYF2019161 and 2019RC221), CAMS Innovation Fund for Medical Sciences (no. 2019-I2M-5-023), Central government for local science and technology (no. ZY2019HN0909), Key Laboratory Open Project Fund of Emergency and Trauma of Ministry of Education (no. KLET-202008).

References

1 L. Y. Ge, R. Hou, Y. Cao, J. C. Tu and Q. Wu, Photoelectrochemical enzymatic sensor for glucose based on Au@C/TiO_2 nanorod arrays, *RSC Adv.*, 2020, **10**(72), 44225–44231.

2 T. Hou, L. F. Zhang, X. Z. Sun and F. Li, Biphasic photoelectrochemical sensing strategy based on *in situ* formation of CdS quantum dots for highly sensitive detection of acetylcholinesterase activity and inhibition, *Biosens. Bioelectron.*, 2016, **75**, 359–364.

3 A. Devadoss, P. Sudhagar, C. Terashima, K. Nakata and A. Fujishima, Photoelectrochemical biosensors: New insights into promising photoelectrodes and signal amplification strategies, *J. Photochem. Photobiol., C*, 2015, **24**, 43–63.

4 T. Xian, H. Yang, L. J. Di and J. F. Dai, Enhanced photocatalytic activity of $SrTiO_3$ particles by surface decoration with Ag nanoparticles for dye degradation, *Phys. Scr.*, 2015, **90**(5), 7.

5 L. P. Wang, Y. Meng, C. X. Zhang, H. B. Xiao, Y. L. Li, Y. M. Tan and Q. J. Xie, Improving Photovoltaic and Enzymatic Sensing Performance by Coupling a Core-Shell Au Nanorod@TiO_2 Heterostructure with the Bioinspired L-DOPA Polymer, *ACS Appl. Mater. Interfaces*, 2019, **11**(9), 9394–9404.

6 A. Bera, K. W. Wu, A. Sheikh, E. Alarousu, O. F. Mohammed and T. Wu, Perovskite Oxide $SrTiO_3$ as an Efficient Electron Transporter for Hybrid Perovskite Solar Cells, *J. Phys. Chem. C*, 2014, **118**(49), 28494–28501.

7 A. Naldoni, U. Guler, Z. X. Wang, M. Marelli, F. Malara, X. G. Meng, L. V. Besteiro, A. O. Govorov, A. V. Kildishev, A. Boltasseva and V. M. Shalaev, Broadband Hot-Electron Collection for Solar Water Splitting with Plasmonic Titanium Nitride, *Adv. Opt. Mater.*, 2017, **5**(15), 11.

8 Z. She, Y. Nie, H. Zhong, L. Liu, S. Yu and Y. Li, Effect of surface deformation on biocompatibility of biomedical alloys, *Mater. Sci. Eng., C*, 2021, **119**, 111636.

9 Y. Onuki, U. Bhardwaj, F. Papadimitrakopoulos and D. J. Burgess, A Review of the Biocompatibility of Implantable Devices: Current Challenges to Overcome Foreign Body Response, *J. Diabetes Sci. Technol.*, 2008, **2**(6), 1003–1015.

10 D. F. Williams, There is no such thing as a biocompatible material, *Biomaterials*, 2014, **35**(38), 10009–10014.

11 H. Dai, Y. H. Zhong, X. Y. Wu, R. X. Hu, L. Wang, Y. C. Zhang, G. K. Fan, X. Y. Hu, J. Li and Z. J. Yang, Synthesis of perovskite-type $SrTiO_3$ nanoparticles for sensitive electrochemical biosensing applications, *J. Electroanal. Chem.*, 2018, **810**, 95–99.

12 W. Xu, W. Yang, H. Guo, L. Ge, J. Tu and C. Zhen, Constructing a TiO_2/PDA core/shell nanorod array electrode as a highly sensitive and stable photoelectrochemical glucose biosensor, *RSC Adv.*, 2020, **10**(17), 10017–10022.

13 H. Lee, S. M. Dellatore, W. M. Miller and P. B. Messersmith, Mussel-inspired surface chemistry for multifunctional coatings, *Science*, 2007, **318**(5849), 426–430.

14 H. J. Nam, B. Kim, M. J. Ko, M. Jin, J. M. Kim and D. Y. Jung, A New Mussel-Inspired Polydopamine Sensitizer for Dye-Sensitized Solar Cells: Controlled Synthesis and Charge Transfer, *Chem.–Eur. J.*, 2012, **18**(44), 14000–14007.

15 L. Romaner, G. Heimel, J.-L. Bredas, A. Gerlach, F. Schreiber, R. L. Johnson, J. Zegenhagen, S. Duhm, N. Koch and E. Zojer, Impact of bidirectional charge transfer and molecular distortions on the electronic structure of a metal-organic interface, *Phys. Rev. Lett.*, 2007, **99**(25), 256801.

16 C. Tyznik, J. Lee, J. Sorli, X. Liu, E. K. Holland, C. S. Day, J. E. Anthony, Y.-L. Loo, Z. V. Vardeny and O. D. Jurchescu, Photocurrent in Metal-Halide Perovskite/Organic Semiconductor Heterostructures: Impact of Microstructure on Charge Generation Efficiency, *ACS Appl. Mater. Interfaces*, 2021, **13**(8), 10231–10238.

17 X. Shi, W. Wang, X. R. Miao, F. Tian, Z. W. Xu, N. Li and M. L. Jing, Constructing Conductive Channels between Platinum Nanoparticles and Graphitic Carbon Nitride by Gamma Irradiation for an Enhanced Oxygen Reduction Reaction, *ACS Appl. Mater. Interfaces*, 2020, **12**(41), 46095–46106.

18 N. Arjona, G. Trejo, J. Ledesma-Garcia, L. G. Arriaga and M. Guerra-Balcazar, An electrokinetic-combined electrochemical study of the glucose electro-oxidation reaction: effect of gold surface energy, *RSC Adv.*, 2016, **6**(19), 15630–15638.

19 R. Long and O. V. Prezhdo, Instantaneous Generation of Charge-Separated State on TiO_2 Surface Sensitized with Plasmonic Nanoparticles, *J. Am. Chem. Soc.*, 2014, **136**(11), 4343–4354.

20 Z. S. Zhang, L. H. Liu, W. H. Fang, R. Long, M. V. Tokina and O. V. Prezhdo, Plasmon-Mediated Electron Injection from Au Nanorods into MoS_2: Traditional *versus* Photoexcitation Mechanism, *Chem*, 2018, **4**(5), 1112–1127.

21 W. Yang, X. Wang, W. Hao, Q. Wu, J. Peng, J. Tu and Y. Cao, 3D hollow-out TiO_2 nanowire cluster/GOx as an ultrasensitive photoelectrochemical glucose biosensor, *J. Mater. Chem. B*, 2020, **8**(11), 2363–2370.

22 T. Hou, N. N. Xu, W. X. Wang, L. Ge and F. Li, Truly Immobilization-Free Diffusivity-Mediated Photoelectrochemical Biosensing Strategy for Facile and Highly Sensitive MicroRNA Assay, *Anal. Chem.*, 2018, **90**(15), 9591–9597.

23 Y. Z. Wei, J. Y. Wang, R. B. Yu, J. W. Wan and D. Wang, Constructing $SrTiO_3$-TiO_2 Heterogeneous Hollow Multi-shelled Structures for Enhanced Solar Water Splitting, *Angew. Chem., Int. Ed.*, 2019, **58**(5), 1422–1426.

24 J. Chen, P. Xiao, J. C. Gu, D. Han, J. W. Zhang, A. H. Sun, W. Q. Wang and T. Chen, A smart hybrid system of Au nanoparticle immobilized PDMAEMA brushes for thermally adjustable catalysis, *Chem. Commun.*, 2014, **50**(10), 1212–1214.

25 M. Steenackers, A. Kuller, S. Stoycheva, M. Grunze and R. Jordan, Structured and Gradient Polymer Brushes from Biphenylthiol Self-Assembled Monolayers by Self-Initiated Photografting and Photopolymerization (SIPGP), *Langmuir*, 2009, **25**(4), 2225–2231.

26 I. Amin, M. Steenackers, N. Zhang, R. Schubel, A. Beyer, A. Golzhauser and R. Jordan, Patterned Polymer Carpets, *Small*, 2011, **7**(5), 683–687.

27 P. Xiao, J. C. Gu, J. Chen, J. W. Zhang, R. B. Xing, Y. C. Han, J. Fu, W. Q. Wang and T. Chen, Micro-contact printing of graphene oxide nanosheets for fabricating patterned polymer brushes, *Chem. Commun.*, 2014, **50**(54), 7103–7106.

28 W. C. Ye, H. Huang, W. W. Yang, X. Wang, C. L. Ren, Q. S. Hu, Y. M. Li and B. Ren, Ultrathin polydopamine film coated gold nanoparticles: a sensitive, uniform, and stable SHINERS substrate for detection of benzotriazole, *Analyst*, 2017, **142**(18), 3459–3467.

29 W. Xu, J. Jia, T. Wang, C. Li, B. He, J. Zong, Y. Wang, H. J. Fan, H. Xu, Y. Feng and H. Chen, Continuous Tuning of Au–Cu_2O Janus Nanostructures for Efficient Charge Separation, *Angew. Chem., Int. Ed.*, 2020, **59**(49), 22246–22251.

30 T. Chen, M. Yang, X. Wang, L. H. Tan and H. Chen, Controlled assembly of eccentrically encapsulated gold nanoparticles, *J. Am. Chem. Soc.*, 2008, **130**(36), 11858–11859.

31 K. Woan, G. Pyrgiotakis and W. Sigmund, Photocatalytic Carbon-Nanotube-TiO_2 Composites, *Adv. Mater.*, 2009, **21**(21), 2233–2239.

32 Y. Horiuchi, T. Toyao, M. Saito, K. Mochizuki, M. Iwata, H. Higashimura, M. Anpo and M. Matsuoka, Visible-Light-Promoted Photocatalytic Hydrogen Production by Using an Amino-Functionalized Ti(IV) Metal-Organic Framework, *J. Phys. Chem. C*, 2012, **116**(39), 20848–20853.

33 W. K. Yang, W. Xu, N. Zhang, X. Y. Lai, J. Peng, Y. Cao and J. C. Tu, TiO_2 nanotubes modified with polydopamine and graphene quantum dots as a photochemical biosensor for the ultrasensitive detection of glucose, *J. Mater. Sci.*, 2020, **55**(14), 6105–6117.

34 H. Mao, J. C. Liang, H. F. Zhang, Q. Pei, D. L. Liu, S. Y. Wu, Y. Zhang and X. M. Song, Poly(ionic liquids) functionalized polypyrrole/graphene oxide nanosheets for electrochemical sensor to detect dopamine in the presence of ascorbic acid, *Biosens. Bioelectron.*, 2015, **70**, 289–298.

35 D. T. Sun, L. Peng, W. S. Reeder, S. M. Moosavi, D. Tiana, D. K. Britt, E. Oveisi and W. L. Queen, Rapid, Selective Heavy Metal Removal from Water by a Metal–Organic Framework/Polydopamine Composite, *ACS Cent. Sci.*, 2018, **4**(3), 349–356.

36 F. Zhang, H. Zhang, R. Chen, Q. Liu, J. Liu, C. Wang, Z. Sun and J. Wang, Mussel-inspired antifouling magnetic activated carbon for uranium recovery from simulated seawater, *J. Colloid Interface Sci.*, 2019, **534**, 172–182.

37 Y. M. Xin, Z. Z. Li and Z. H. Zhang, Photoelectrochemical aptasensor for the sensitive and selective detection of kanamycin based on Au nanoparticle functionalized self-doped TiO_2 nanotube arrays, *Chem. Commun.*, 2015, **51**(85), 15498–15501.

38 F. Yu, S. G. Chen, Y. Chen, H. M. Li, L. Yang, Y. Y. Chen and Y. S. Yin, Experimental and theoretical analysis of

polymerization reaction process on the polydopamine membranes and its corrosion protection properties for 304 Stainless Steel, *J. Mol. Struct.*, 2010, **982**(1–3), 152–161.

39 X. Zhou, J. Y. Shi and C. Li, Effect of Metal Doping on Electronic Structure and Visible Light Absorption of $SrTiO_3$ and $NaTaO_3$ (Metal = Mn, Fe, and Co), *J. Phys. Chem. C*, 2011, **115**(16), 8305–8311.

40 W. K. Yang, W. Xu, Y. D. Wang, D. L. Chen, X. H. Wang, Y. Cao, Q. Wu, J. C. Tu and C. Zhen, Photoelectrochemical Glucose Biosensor Based on the Heterogeneous Facets of Nanocrystalline TiO_2/Au/Glucose Oxidase Films, *ACS Appl. Nano Mater.*, 2020, **3**(3), 2723–2732.

41 B. D. Yan, Y. Zhuang, Y. L. Jiang, W. Xu, Y. J. Chen, J. C. Tu, X. H. Wang and Q. Wu, Enhanced photoelectrochemical biosensing performance from rutile nanorod/anatase nanowire junction array, *Appl. Surf. Sci.*, 2018, **458**, 382–388.

42 X. Q. Liu, X. H. Huo, P. P. Liu, Y. F. Tang, J. Xu, X. H. Liu and Y. M. Zhou, Assembly of MoS_2 nanosheet-TiO_2 nanorod heterostructure as sensor scaffold for photoelectrochemical biosensing, *Electrochim. Acta*, 2017, **242**, 327–336.

43 S. Selvarajan, N. R. Alluri, A. Chandrasekhar and S. J. Kim, $BaTiO_3$ nanoparticles as biomaterial film for self-powered glucose sensor application, *Sens. Actuators, B*, 2016, **234**, 395–403.

44 W. J. Wang, L. Bao, J. P. Lei, W. W. Tu and H. X. Ju, Visible light induced photoelectrochemical biosensing based on oxygen-sensitive quantum dots, *Anal. Chim. Acta*, 2012, **744**, 33–38.

45 M. X. Shang, H. Qi, C. C. Du, H. Huang, S. Y. Wu, J. L. Zhang and W. B. Song, One-step electrodeposition of high-quality amorphous molybdenum sulfide/RGO photoanode for visible-light sensitive photoelectrochemical biosensing, *Sens. Actuators, B*, 2018, **266**, 71–79.